ChemPhysChem

Research Article
doi.org/10.1002/cphc.202400420

Chemistry Europe
European Chemical Societies Publishing

www.chemphyschem.org

Optical and Supramolecular Properties of Cyclometalated Palladium Nanostructures with Tumor Targeting Properties in Living Mice: A Quantum Mechanics Interpretation.

Costantino Zazza,*[a] Nico Sanna,[a, b] Stefano Borocci,[a, c] and Felice Grandinetti[a, c]

The recent discovery that metallophilic interactions between cyclometalated palladium supramolecular nanostructures – with efficient tumour accumulation rate in a skin melanoma model – maintain excellent photodynamic properties even in a hypoxic microenvironment has inspired the present study focused on the theoretical predictions of optical properties of the bis-cyclometalated palladium compound in different contexts. More specifically, structural and UV/Vis absorption properties of both monomeric and dimeric forms of this anticancer drug are well reproduced with a Time-Dependent Density Functional Theoretical (TD-DFT) approach based on Exchange–Correlation (XC) hybrid functionals in conjunction with conductor-like and polarization solvation effects. A further novelty is represented by a fine investigation of the supramolecular interactions between the different subunits of the drug via dispersion force correction and Quantum Theory of Atoms in Molecules (QTAIM). This contribution while supporting the photoexcitation properties derived in laboratory following the self-assembly of monomeric units when passing from dimethyl sulfoxide (DMSO) to a H_2O/DMSO mixture at 298 K, shed some light on the nature of the chemical interactions modulating the formation of nano-size aggregates.

1. Introduction

Organometallic compounds are well established pivotal players in current chemistry.[1,2] Illustrative examples include the (half−) sandwich compounds also known as piano stool complexes,[3–5] the transition metal carbenes with ferrocene,[6] and the Grubbs-type catalysts.[7,8] In the last decades, compounds like these have found vast applications in catalysis and biosensing with a wide use in commercial reactions and related processes.[9–11] Organometallic compounds are also largely applied nowadays as medicinally-relevant drugs, belonging essentially to three classes: 1) antimicrobial organoarsenicals; 2) antimalarial and anticancer ferrocene-containing compounds; 3) anticancer catalytic organometallic complexes.[12,13] In this respect, traditional chemotherapy applications, characterized by the use of small organic molecules, have undoubtedly made significant strides in cancer treatments.[14,15] However, the non-selective nature of many chemotherapeutic agents often leads to severe side effects, compromising the quality of life for patients.[16,17] In some cases, catalytic anticancer metallodrugs result active even at low doses minimizing potential side-effects and, at the same time, are found to introduce novel mechanisms of action against resistance towards anticancer-drug activities.[18] The integration of metals into therapeutic compounds brings forth a diverse range of mechanisms of action, allowing for tailored approaches to combat the heterogeneity of cancer. Metal complexes can interfere with essential cellular processes, such as DNA replication and repair, induce apoptosis, or modulate signaling pathways critical for cancer cell survival.[19] The unique electronic and structural properties of organometallic compounds offer a platform for the design of agents with enhanced selectivity and reduced toxicity, marking a paradigm shift in the landscape of antitumor drug development.[20] The precise understanding of the factors governing the stability and reactivity of organometallic complexes remains a subject of intense investigation. The exploration of new synthetic methodologies and the design of compounds with tailored properties are also posing exciting avenues for further researchers. This aspect actually has open up the routes for the development of intriguing approaches to cancer therapy. Among these fascinating applications, a further strategy has emerged to treat tumors based on tumor-targeting (covalently or supramolecularly) nanocarriers which enhances drug delivery to the tumoral cells in clinical applications.[21–23] Another intriguing approach to cancer therapy involves the use of relatively small-molecule drugs that self-assemble into supramolecular nanostructures without the assistance of nanocarriers.[24,25] In this respect, although these systems can be synthesized quite easily, the

[a] C. Zazza, N. Sanna, S. Borocci, F. Grandinetti
Department for Innovation in Biological, Agro-food and Forest systems (DIBAF), Università della Tuscia, L.go dell'Università, s.n.c., 01100 Viterbo, Italy
E-mail: costantino.zazza@unitus.it

[b] N. Sanna
Istituto per la Scienza e Tecnologia dei Plasmi (ISTP) del CNR, Via G. Amendola 122/D, 70126 Bari, Italy

[c] S. Borocci, F. Grandinetti
Istituto per i Sistemi Biologici (ISB) del CNR, Sede di Roma – Meccanismi divReazione c/o Dipartimento di Chimica, Sapienza Università di Roma, P.le A. Moro 5, 00185 Rome, Italy

Supporting information for this article is available on the WWW under https://doi.org/10.1002/cphc.202400420

non-covalent forces driving the self-assembly among individual molecules should be able to guarantee the survival of these nanostructures in living organism under physiological conditions. Such Drug Self-Delivery Systems (DSDSs) must be then optimized in terms of a complex balance between hydrophobic forces, supramolecular contacts and/or Metal-Ligand (M–L) coordination patterns. In a recent study, Zhou et. el.[26] first proposed cyclometalated palladium-based (PdL, see Scheme 1) supramolecular nanostructures, which show efficient tumour accumulations rates (up to 10.2% ID g^{-1} and circulation time peaks at 12 h in living mice) in a skin melanoma, e.g. *A375*, in living mice. The proposed organometallic compound results from the interaction of a mixture of bis(3-(pyridin-2-yl)phenyl)amine, reported in literature as H_2L, with Palladium(II) acetate, $Pd(OAc)_2$. It was shown[26] that the PdL supramolecular aggregates maintain excellent photodynamic properties even in hypoxic tumour microenvironment.[27,28] The surprising observation that green light irradiation of PdL nanostructures leads to tumour destruction due to photodynamic type-I reactivity in vivo strongly suggest potentially relevant applications in clinical photodynamic therapy (PDT).[29–32] A light-activated anticancer drug such as PdL with a remarkable selectivity and long circulation time offer a patient-friendly alternative to traditional chemotherapy while reducing side effects by a selective irradiation of tumour tissue.

The PdL complexation generating photo-responsive supramolecular nanostructures in living mice is supposed to be driven by metallophilic interactions involving the Pd atoms. Metallophilic interactions are, generally, defined as non-covalent forces between d^8 and d^{10} transition metal ions such as Pd(II), Pt(II), Au(I), Ag(I), and Cu(I) actually enhanced by relativistic effects and electron correction of the closed-shell constituents.[32–34] In these interactions the repulsive metal-metal Pauli component is *de facto* suppressed by the linear coordination geometries of the complexes; this brings to relatively close M···M distances shorter than the sum of the van der Waals radius. Particularly for PdL, the role of metallophilic interactions (modulated also by solvation effects) in driving one-dimensional assembly during dimerization (see Scheme 1) is highlighted by the X-ray structures in DMSO/H_2O mixtures of the PdL-Dimer, $(PdL)_2$, featuring Pd–Pd distances of 3.518 Å, and a short interplanar average distance of ca. 3.4 Å.[26] This finding reinforces the expectation that metallophilic interactions play a major role in driving the supramolecular assembly of nanoarchitectures in multi-component systems under different environments.[34]

In the present study, we performed *ab-initio*[35] and density functional theory (DFT)[36] calculations to investigate the structure and spectroscopic properties of both naked and solvated PdL and $(PdL)_2$. The bonding situation of these systems was also assayed by different methods of bonding analysis. The obtained data favorably compare with experimental measurements and previous calculations, and at the same time shed some new light on the structural and electronic properties of these intriguing organometallic systems.

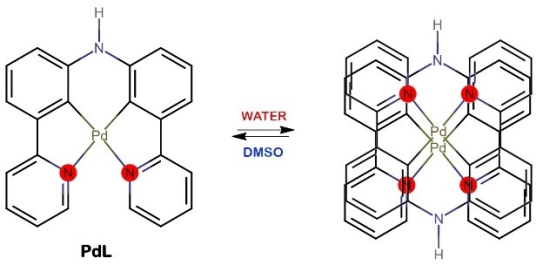

Scheme 1. Chemical structure of the PdL organometallic compound (monomeric and dimeric form). In pure DMSO, PdL (100 μM) was observed mostly in the monomeric form while in the presence of DMSO/Water mixtures ~10%, e.g. 1/9, the formation of Pd···Pd supramolecular contacts in solution is preferred as observed by Transmission Electron Microscopy (TEM) and emission spectroscopic measurements at room-temperature.[26]

2. Theoretical Methods and Computational Details

DFT calculations were performed using three different gradient corrected approximation-based (GGA) functionals[37]: the pure exchange-correlation Perdew–Burke-Ernzerhof (PBE) functional,[38] the hybrid PBE0 functional[39] mixing the PBE exchange energy and Hartree–Fock (HF) exchange energy in a 3:1 ratio, along with the full PBE correlation energy, and the hybrid Becke 3-parameters Lee–Yang–Parr (B3LYP) functional.[40–42] We also used with any functional the Grimme's dispersion with the original D3 damping function which adds an empirical function akin to the Lennard-Jones potentials and systematically improves the description of van der Waals systems.[43] The H, C, and N atoms were treated with the Dunning's correlation consistent-polarized cc-pVTZ basis sets,[44] and the Pd atoms were treated with the corresponding basis developed in conjunction with effective core pseudopotential (PP) (cc-pVTZ-PP).[45] Both these basis sets will be henceforth denoted as VTZ. Full electron calculations with a relativistic Hamiltonian were also performed within the second-order Douglas-Kroll-Hess (DKH2) approximation.[46,47] The investigated systems were relaxed by applying a redundant-based internal coordinates algorithm in dilute solution mimicking the dimethyl sulfoxide (DMSO) and water solvent effects by using the popular Conductor-like Polarizable Continuum Model (C-PCM) decomposition.[48] The taken reaction-field approach allows to maintain a DFT picture of PdL and $(PdL)_2$ while introducing solvation and polarization effects in a self-consistent way within the Kohn-Sham equations. The C-PCM/[PBE;B3LYP;PBE0]/VTZ geometries were then employed to calculate the UV-Vis absorption spectra – in the range 290–800 nm – by combining vertical excitation energies with oscillator strengths and using gaussian broadening functions having a full width at half maximum (FWHM) of 3000 cm^{-1} (*i.e.* the $\Delta\nu'_{1/2}$). The formula employed by the GaussSum software[49] used to convolute the computed absorption spectra is given below:

$$\varepsilon(\nu') = \frac{2.175 \cdot 10^8}{\Delta\nu'_{\frac{1}{2}}} \cdot f \cdot exp\left[-2.772 \cdot \frac{(\nu' - \nu'_{i\to f})^2}{\Delta\nu'_{\frac{1}{2}}}\right] \quad (1)$$

where f (the oscillator strength under the transition dipole length approximation) and $\nu'_{i\to f}$ (the vertical excitation energy in wavenumbers, cm^{-1}) are both extracted from quantum mechanical calculations at TD-DFT level of theory.[50] The oscillator strength is related to the transition dipole moment, $M_{i\to f}$ by the equation:

$$f_{i\to f} = \frac{8\ \pi\ m_e}{3\ e^2\ h^2} \cdot \Delta E_{i\to f} \cdot \ |M_{i\to f}|^2 = \frac{8\ \pi\ m_e\ c}{3\ e^2\ h^2} \cdot \nu'_{i\to f} \cdot \ |M_{i\to f}|^2 \quad (2)$$

where m_e and e are the mass and the charge of the electron, respectively, h is Planck's constant and c is the speed of light.

The energy difference ($\triangle E_{i\to f}$) between these states is related to the frequency ν, the wavelength λ and the wavenumber ν' of absorbed or emitted light by the equation:

$$\Delta E_{i\to f} = h \cdot \nu_{i\to f} = h \cdot \frac{c}{\lambda_{i\to f}} = \ h \cdot c \ \cdot \nu'_{i\to f} \quad (3)$$

The results of a TD-DFT calculations may be then convoluted using gaussian-type curves to create UV/Visible spectra; more specifically, each electronic transition is associated with a gaussian curve accordingly to the expression of the $\varepsilon(\nu')$ value which provides an estimation of the molar absorption coefficient, in $M^{-1}\ cm^{-1}$, as reported in Equation (1). Next, the emerging curves are summed along a one-dimensional grid, composed by 500 points in the range between 290–800 nm, to generate the overall spectrum. Moreover, the molecular orbitals involved in the Franck-Condon excitation processes were characterized in terms of electronic hypersurfaces superimposed to the optimized structures. All the calculations were performed with the Gaussian 16 code (Rev. C01),[51] using the VMD software[52] to depict the molecular geometries.

The bonding analysis of the $(PdL)_2$ was accomplished using the Bader's theory of atoms in molecules (AIM).[53] The employed method was the Møller-Plesset perturbation theory truncated at the second order (MP2)[54] used in conjunction with the VTZ basis set. The analyzed functions include the electron density $\rho(\boldsymbol{r})$, the electron energy density $H(\boldsymbol{r})$ and its kinetic and potential components $G(\boldsymbol{r})$ and $V(\boldsymbol{r})$, respectively and the reduced density gradient (RDG) $s(\boldsymbol{r})$. The $\rho(\boldsymbol{r})$ is defined by the equation[53]:

$$\rho(\boldsymbol{r}) = \sum_i \eta_i |\varphi_i(\boldsymbol{r})|^2 \quad (4)$$

where η_i is the occupation number of the natural orbital φ_i, in turn expanded as a linear combination of the basis functions. The $H(\boldsymbol{r})$ is the sum of the kinetic energy density $G(\boldsymbol{r})$ and the potential energy density $V(\boldsymbol{r})$:

$$H(\boldsymbol{r}) = G(\boldsymbol{r}) + \ V(\boldsymbol{r}) \quad (5)$$

The presently-employed definition[53] of the $G(\boldsymbol{r})$ is given by the equation:

$$G(\boldsymbol{r}) = \frac{1}{2}\sum_{i=1} \eta_i |\nabla\varphi_i(\boldsymbol{r})|^2 \quad (6)$$

where the sum running over all the occupied natural orbitals φ_i of occupation numbers η_i. The potential energy density $V(\boldsymbol{r})$ is evaluated[53] from the local form of the virial theorem:

$$V(\boldsymbol{r}) = \frac{1}{4}\nabla^2\rho(\boldsymbol{r}) - 2G(\boldsymbol{r}) \quad (7)$$

The RDG – coming from the density and its first derivative – is defined by the equation[55,56]

$$s(\boldsymbol{r}) = \frac{|\nabla\rho(\boldsymbol{r})|}{2(3\pi^2)^{\frac{1}{3}} \times \rho(\boldsymbol{r})^{\frac{4}{3}}} \quad (8)$$

Low-value $s(\boldsymbol{r})$ isosurfaces (typically 0.3–0.6) appear among atoms undergoing any type of interaction, the Non-Covalent Interactions (NCIs) emerging, in particular, by considering the spatial regions of low $\rho(\boldsymbol{r})$ (typically at around 0.05 $e{\cdot}a_0^{-3}$). The low-$s(\boldsymbol{r})$/low-$\rho(\boldsymbol{r})$ isosurfaces are, in turn, mapped in terms of the $sign(\lambda_2){\times}\rho(r)$, λ_2 being the second eigenvalue ($\lambda_1 < \lambda_2 < \lambda_3$) of the Hessian matrix of $\rho(\boldsymbol{r})$. In essence, the sign of λ_2 is used to distinguish between attractive ($\lambda_2 < 0$) and repulsive ($\lambda_2 > 0$) interactions, and the value of $\rho(\boldsymbol{r})$ is exploited to rank the corresponding strength. Thus, the NCIs are conveniently visualized in a 2D plane by plotting the RDG *vs* the colored $sign(\lambda_2){\times}\rho(r)$, and in 3D space by plotting a chosen low-value isosurface of the $s(\boldsymbol{r})$, colored by the $sign(\lambda_2){\times}\rho(r)$ (standard employed colors range from blue to red for highly attractive to repulsive interactions, respectively). The analysis was done with the Multiwfn program (version 3.8.dev)[57] using the wfx files generated with Gaussian 16 code.[51] The 2D and 3D plots of the $s(\boldsymbol{r})$ *vs* $sign(\lambda_2){\times}\rho(r)$ were produced with the VMD software[57] setting $sign(\lambda_2){\times}\rho(r)$ between -0.050 $e{\cdot}a_0^{-3}$ (blue) and 0.010 $e{\cdot}a_0^{-3}$ (red). The MP2/aVTZ electrostatic potential energy surfaces (ESP) were also calculated using the wavefunctions generated by the Gaussian code, and by applying the Libreta algorithm[58] integrated into Multiwfn program. At last, we also investigated the $(PdL)_2$ system in its lowest-energy triplet spin multiplicity with the target of addressing structural changes activated by relaxation dynamics along electronic excited states.

3. Results and Discussion

3.1. Optimized Structures and Optical Properties

The structures of the $(PdL)_2$ obtained with our three employed DFT methods [B3LYP(D3), PBE0(D3) and PBE(D3)] were com-

pared with the X-ray crystallographic data and with previous calculations at PBE0/TZP level.[26] A benchmark parameter in this regard is the Pd–Pd distance. The crystallographic value of 3.52 Å is underestimated as 3.26 Å by previous calculations in methanol dilute solution.[26] Our obtained values are, instead, closer to the experimental one. The best-performing level is the B3LYP/(D3)/VTZ, which predicts a Pd–Pd distance of 3.54 Å in vacuum, and 3.60/3.61 Å in DMSO/water (see Figure 1a and b). The PBE0 predicts a Pd–Pd distance of 3.68 Å in DMSO and 3.67 Å in water, and the pure PBE furnishes a value of 3.72 Å in both DMSO and water. The ESP of PdL and $(PdL)_2$ are given in Figure 1c–e. Electrophilic sub-units in DMSO are represented by blue color indicating negative regions and are located – as it would have been expected – on more electronegative atoms. Positive portions (red color) instead correspond to nucleophilic regions suggesting– on average – a lack of electrons. The highest potential energy region, with a value of +0.16 a.u., is located around the N–H group which makes this position prone to nucleophilic attack. The observed trend also highlights that ligand loses planarity due to the repulsion between N–C–H—H–C–N intramolecular moieties. As a consequence, for both the systems, the ESP surface in proximity of these two terminal portions reflect a reduced electrophilic reactivity if compared with the remaining planar region of the PdL ring. In this respect, the perfectly planar structure (C_s symmetry) is slightly less stable by 0.16 kcal/mol (at C-PCM/B3LYP(D3)/VTZ level of theory in DMSO). This ESP-based characterization of PdL in terms of electron-rich and -deficient regions provides a self-consistent prediction about its interaction with encircling solvent molecules. Also, we obtained a similar result introducing the PdL and $(PdL)_2$ molecules in water.

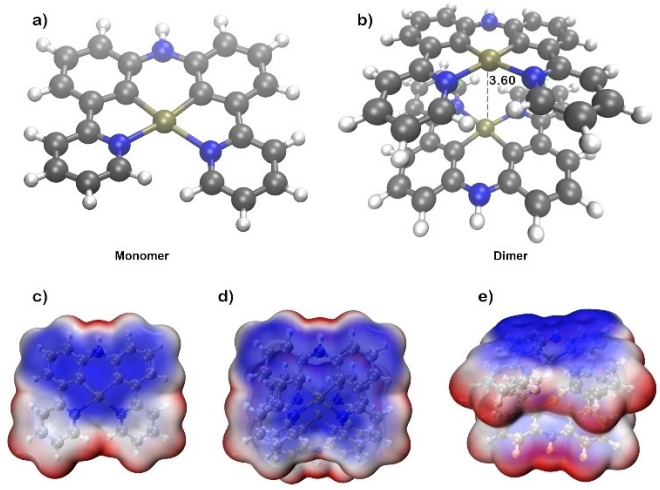

Figure 1. Geometrical structures of the two organometallic systems. a) the PdL molecule (C atoms are in gray, Pd in yellow, N in blue and H in white colour, respectively); b) the PdL molecule forming the dimer with the Pd–Pd distance reported in Å. The structures depicted are extracted from optimized geometries at B3LYP(D3)/VTZ level of theory in DMSO dilute solution simulated by C-PCM implicit model. At the same level of theory the molecular electrostatic potential (ESP, isodensity value of 0.03 a.u.) surfaces are also reported for the monomeric (c) and for the dimeric form (d and e) in DMSO; the blue and red points represent the local minima (−0.9 a.u.) and maxima (0.16 a.u.) values of the ESP surface, respectively.

As a next step, we focused on the UV/Vis absorption of PdL and $(PdL)_2$ in DMSO and water, explicitly investigated by Zhou et. al.[26] In DMSO, the experimental spectrum includes – in the range 300–800 nm – three absorption bands with a maximum at 343 nm ($\varepsilon = 25.8\times10^3\ M^{-1}\,cm^{-1}$) and two signals at longer wavelengths centered at 405 nm ($\varepsilon = 5.2\times10^3\ M^{-1}\,cm^{-1}$) and 481 nm ($\varepsilon = 3.7\times10^3\ M^{-1}\,cm^{-1}$), respectively. TD-DFT/PBE0/TZP/COSMO calculated spectra of PdL in methanol dilute solution[26] essentially suggested that in pure DMSO only the monomer should be present, but unfortunately, the predicted absorption patterns resulted confined at excitation wavelengths lower than 390 nm. The observed discrepancy between measured and estimated spectra intrigued as. The same authors also observed that supramolecular dimerization shifts the lowest-energy absorption band from 383 nm to 502 nm. However, the observed trend strongly suggested that, at PdL concentration within 100 μM, the organometallic complex in DMSO tends to avoid aggregating towards supramolecular nanostructures driven by metallophilic interactions. As a result, a spectral region of the UV/Vis spectra of the PdL molecule still should be further clarified. To this end, in Figure 2 we show the calculated UV/Vis absorption patterns both for monomeric and dimeric form of PdL in a DMSO dilute environment. As for the monomer, PBE0 and B3LYP functionals feature excitation wavelengths close to the experimental measurements (see Figure 1, upper panel). When the PdL is dissolved in DMSO, the PBE0 functional predicts a lowest-energy signal at 466 nm ($\varepsilon = 4.1\times10^3\ M^{-1}\,cm^{-1}$) accompanied by a second absorption peak at 400 nm ($\varepsilon = 3.3\times10^3\ M^{-1}\,cm^{-1}$) and a prominent band centered at 336 nm ($\varepsilon = 35.1\times10^3\ M^{-1}\,cm^{-1}$). The molecular orbitals involved in the excitation process are depicted in Figure 3a.

The electronic transition at 466 nm reflects a $^1\pi\rightarrow\pi^*$ character mainly being a HOMO(H)→LUMO(L) (96%) excitation. Afterwards, we observe that also the signal detected at 400 nm features a valence $^1\pi\rightarrow\pi^*$ excitation character [*i.e.*, H→L+1 (95%)]. At last, the main absorption band centered at 366 nm results essentially from the convolution of a H-3→L (44%), H-2→L (24%), H→L+3 (28%) excitation with an oscillator strength (f) of 0.27 a.u. and a H-1→L (58%), H→L+2 (37%) second excitation with f = 0.13 a.u. We are, indeed, again mainly referring to a valence $^1\pi\rightarrow\pi^*$ absorption band. The same signals result estimated at 489 nm ($\varepsilon = 3.8\times10^3\ M^{-1}\,cm^{-1}$), 425 nm ($\varepsilon = 2.5\times10^3\ M^{-1}\,cm^{-1}$), and 352 nm ($\varepsilon = 30.6\times10^3\ M^{-1}\,cm^{-1}$) by using the hybrid B3LYP functional. It is worth noting that, similar results were obtained using an all-electrons approach with a relativistic Hamiltonian: an absorption at 494 nm ($\varepsilon = 3.1\times10^3\ M^{-1}\,cm^{-1}$), a second band at 421 nm ($\varepsilon = 2.9\times10^3\ M^{-1}\,cm^{-1}$) and a prominent peak at 350 nm ($\varepsilon = 27.3\times10^3\ M^{-1}\,cm^{-1}$). On the other hand, the pure PBE functional provides a different shape of the spectrum, including two absorption bands, and overestimates the excitation wavelengths. The lowest-energy absorption is centered at almost 660 nm ($\varepsilon = 3.1\times10^3\ M^{-1}\,cm^{-1}$) and the main signal at 436 nm ($\varepsilon = 19.1\times10^3\ M^{-1}\,cm^{-1}$). As a next step, in Figure 3b we report a comparison between the computed absorption pathways and the experimental ones in DMSO at 298 K. The agreement between computations and experiments is very good in all the

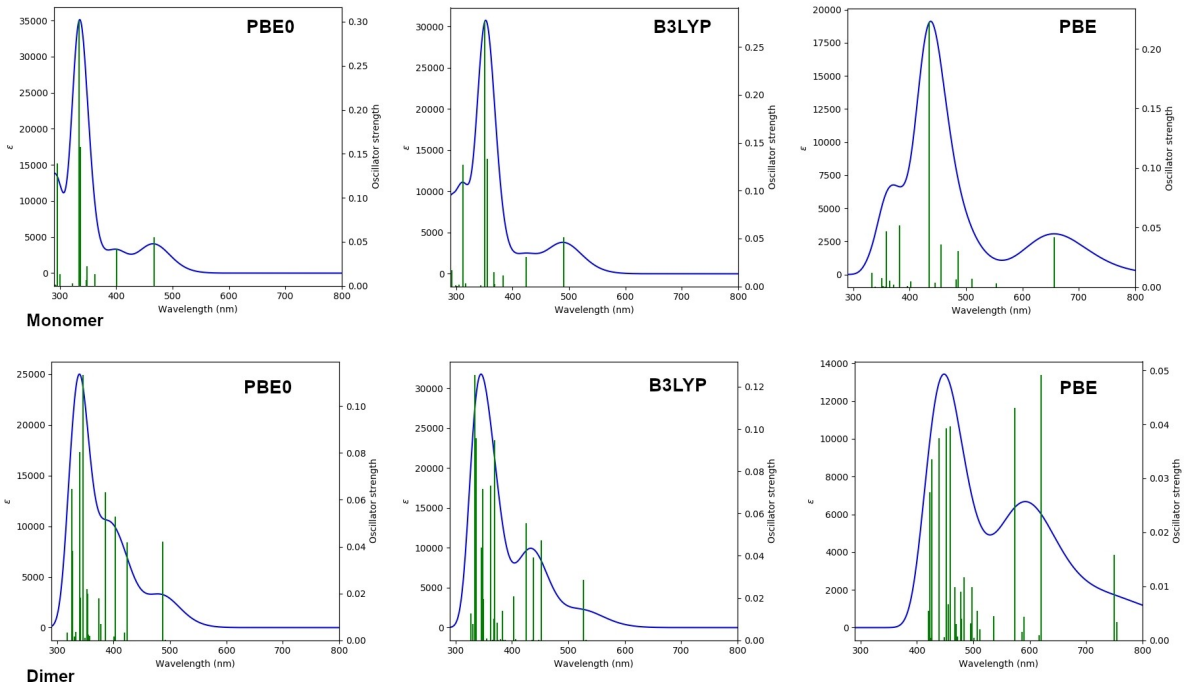

Figure 2. UV/Vis absorption spectra for the monomeric (upper panel) and dimeric form (lower panel) of the PdL organometallic compound in DMSO dilute environment at C-PCM/PBE0(D3)//B3LYP(D3)//PBE(D3)/VTZ level of computations. The molar absorption coefficient (ε) is reported in M^{-1} cm^{-1}. Oscillator strengths (in a.u.) are also reported as green histograms.

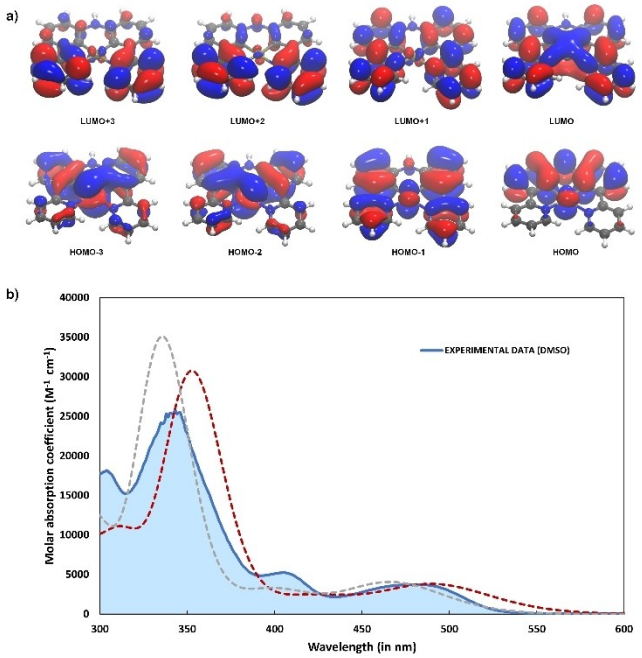

Figure 3. a) Molecular orbitals, at C-PCM/PBE0(D3)/VTZ level, for the PdL monomer in DMSO. The blue colour reflects the positive (+) part of the corresponding eigenvector and an isodensity value of 0.015 $e\ a_0^{-3}$ is used; b) Computed (C-PCM/B3LYP red dashed line; C-PCM/PBE0 gray dashed line) UV/Vis absorption spectra of PdL compound in DMSO mainly in its monomeric form following the experimental observations. The experimental spectrum is taken from the ESI.[26] The solution solvating PdL is treated at C-PCM level of decomposition, and the convoluted profiles are estimated with gaussian broadening functions having a FWHM of 3000 cm^{-1}.

range of wavelengths. The positions of the computed absorption bands as well as the shape of the emerging spectra strongly resemble the trends observed experimentally. In light of this, our result strongly supports the evidence that PdL molecules, in a solvent like the DMSO, tend to be preferentially widespread as monomeric species in solution. For the dimeric form – always in DMSO – we observe that also in this case PBE0 and B3LYP estimate essentially a similar behavior; the absorption spectra show a marked increase in the baseline due to the presence of multiple singlet electronic excitations falling in the same intervals. At C-PCM/PBE0(D3)/VTZ level of theory, the emerged UV/Vis spectrum shows a first band at 478 nm ($\varepsilon = 3.0\times10^3\ M^{-1}cm^{-1}$), a main peak at 341 nm ($\varepsilon = 17.0\times10^3\ M^{-1}cm^{-1}$) with a shoulder located at 377 nm ($\varepsilon = 9.5\times10^3\ M^{-1}cm^{-1}$). With the B3LYP functional, the same signals are predicted at 526 nm, 438 nm and 346 nm while they are shifted at lower energies applying the PBE functional (see Figure 2, lower panel). The molecular orbitals involved in the excitations are shown in Figure 4a. The lowest $^1\pi\rightarrow\pi^*$ excitation at 526 nm features a H-1→L (94%) composition (f = 0.04). The shoulder at 377 nm is mainly composed by three $^1\pi\rightarrow\pi^*$ vertical excitations falling at 428 nm [H→L + 1 (92%); f = 0.04)], 409 nm [(H→L + 2 (92%), H-1→L + 3(5%); f = 0.05)], and 390 nm [(H-2→L (90%), H-7→L + 1 (2%), H-4→L(2%); f = 0.06)]. At last, the main $^1\pi\rightarrow\pi^*$ absorption signal in the range 300–800 nm results essentially composed by an excitation lying at 348 nm [H-5→L(66%), H-1→L + 4(13%), H-4→L(6%); f = 0.13], with two H-excitation having a multiple character and estimated at 342 nm 1→L + 7(3%), H→L + 5(9%); f = 0.08)] and 328 nm [H-1→L + 6 [(H-6→L (60%), H-4→L + 1(5%), H-1→L + 5(4%), H-1→L +

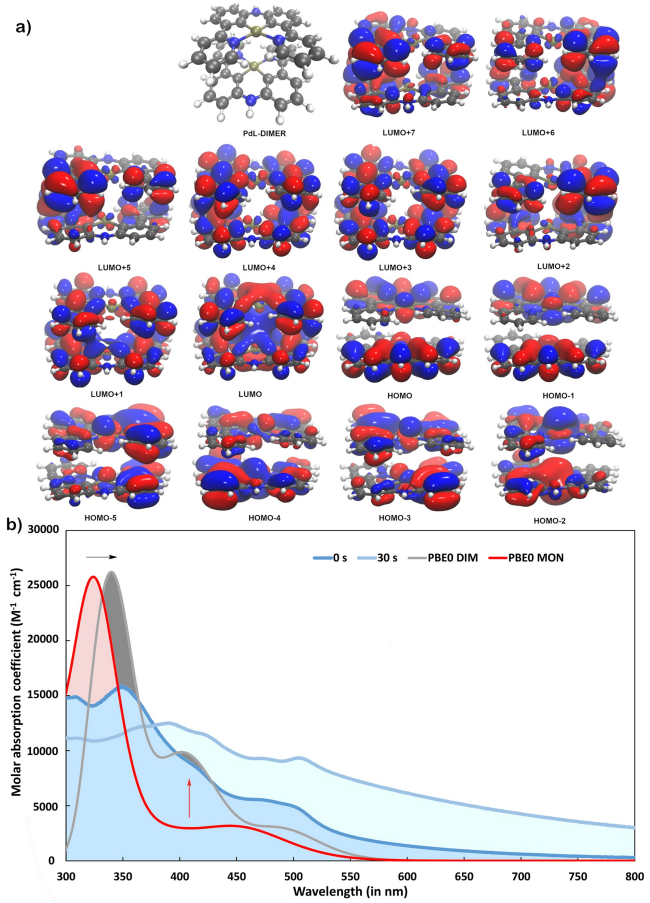

Figure 4. a) Molecular orbitals, as extracted at C-PCM/PBE0(D3)/VTZ level, for the PdL in the stable dimeric form in DMSO dilute solution. The blue colour reflects the positive (+) counterpart of the corresponding eigenvector and an isodensity surface plot value of 0.015 $e\ a_0^{-3}$ is represented. b) UV/Vis absorption spectra [experimental data *vs* theoretical prediction [C-PCM/PBE0(D3)/VTZ] of PdL in H_2O solution in its monomeric and dimeric form, respectively. The transient experimental UV/Vis absorptions at 0 s (blue solid line) and 30s (light-blue solid line) are taken from the ESI of Ref.[26]

6(8%), (75%), H-7→L (5%), H-6→L(6%), H-1→L+7 (3%), H→L+7 (3%); f=0.06], respectively.

Also in the present context, the DFT(D3)-based UV/Vis spectra that have emerged at PBE0 and B3LYP (see Figure 2, lower panel) result in agreement with experimental observations in which the supramolecular dimerization is supposed to play a key role in modulating the absorption patterns.[26] In this context, minute variations in the UV/Vis spectrum of PdL in DMSO with temperature, suggested low-affinity dimerization with constant of 10^{-3}–10^{-4} M^{-1}. To further deepen the comparison with the experimental data, we have reported, in Figure 4b, four different spectra: the transient experimental UV/Vis absorptions at 0 s (blue solid line) and 30s (light-blue solid line)[26] for the PdL in water and the computed aqueous absorption patterns for the monomer and dimer of PdL. The transient spectra of 100 μM of PdL at 0 s was associated to the relatively low presence of supramolecular dimeric structures while that recorded at 30s to the presence of stable supramolecular nanostructures. In this respect, we have modeled the presence of nanostructures by means of dimeric forms of PdL. As it can be clearly seen from the estimated trend (Figure 4b), the self-assembly of such a light activated anticancer drug strongly affects the photophysical properties in aqueous dilute solutions. As a matter of fact, there is a remarkable change in the absorption spectra which can be directly associated with nanostructure formations. When passing from monomer to dimer, supramolecular interactions between PdL units are capable of shifting the excitations towards lower energies while increasing the baseline of the spectra. In this respect, our computations show that, in aqueous environment, the formation of supramolecular structures, stabilized by metallophilic interactions, is accompanied by a red-shift of the excitation patterns of PdL molecules. Interestingly, computations also well reproduce the drastic increase in the absorption process experimentally detected at around 410 nm due to the appearance of multiple valence $^1\pi\rightarrow\pi^*$ absorption signals (see Figure 4a). In agreement with previous investigation,[26] the influence of self-assembly finely modulated by environmental effects has therefore a deep impact on photophysical properties of PdL organometallic compounds.

3.2. Bonding Patterns of $(PdL)_2$

The nature of the interlayer contacts occurring in $(PdL)_2$ was assayed by an QTAIM analysis. In this context, we would like to mention that several contributions had already addressed the potentialities of theoretical relativistic approximations within the QTAIM decomposition model.[59] The relevant results are given in Figure 5 and in Table 1. Irrespective of the environment (gas, DMSO, water), the region between the two layers includes numerous $\rho(r)$ critical points of the type (+3,−1). As shown in Figure 5a, for the gas-phase complex, two of these BCPs belong to bond paths (BPs) connecting a H atom of one layer with a C atom of the other one; all the other BCPs belong to BPs connecting pairs of C atoms. The Pd–Pd BP is also located. The C–H BPs are not occurring in DMSO and water, the only BPs located in these environments being the Pd–Pd and the C–C ones. Thus, at least in terms of the topology of the $\rho(r)$, the N atoms of the two layers do not contribute to the stability of the dimer. The AIM indices computed for the various BCPs, reported in Table 1, clearly unravel the non-covalent nature of any contact occurring between the two layers. At any BCP, in fact, the $\rho(r)$ is within 0.01 $e{\cdot}a_0^{-3}$, the $\nabla^2\rho(r)$ and the $H(r)$ are positive, and the $-G(r)/V(r)$ ratio is greater than one. The Pd–Pd bond path is the relatively strongest one, with a ρ(BCP) of 0.0102 $e{\cdot}a_0^{-3}$ in the gaseous complex, and of ca. 0.009 $e{\cdot}a_0^{-3}$ in DMSO and water. The $\rho(BCP)$ of all the other contacts ranges between *ca.* 0.004 and *ca.* 0.007 $e{\cdot}a_0^{-3}$, the interactions occurring in the gaseous phase being, generally, tighter than the corresponding ones occurring in the solvated complexes. The nature of the solvent produces also minor differences, if any, on the AIM indices of the various corresponding BCPs. The non-covalent character of the interactions stabilizing the $(PdL)_2$ is also clearly caught by examining the results obtained from the study of the RDG. The RDG is a fundamental dimensionless quantity in theoretical chemistry typically used to describe the deviation

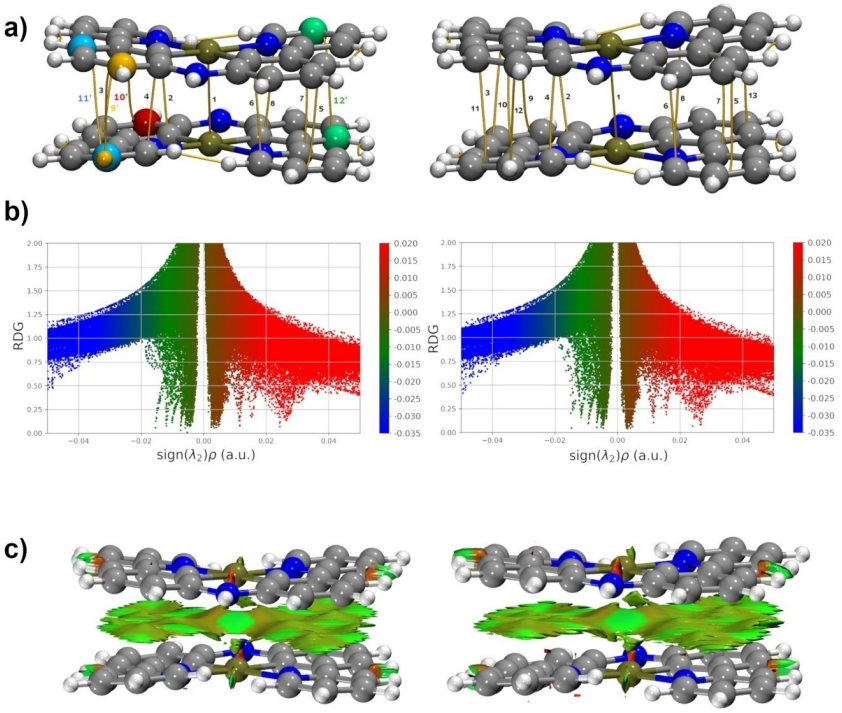

Figure 5. a) Bond paths at MP2/VTZ level of theory (see section 2) for the $(PdL)_2$ in gas phase (left panel) and in DMSO dilute solution (right panel); b) 2D Reduced Density Gradient plot in which the color bar represents the $sign(\lambda_2)\times\rho(r)$ in a. u.; c) 3D Reduced Gradient Density plot [also in this case, the color bar represents the $sign(\lambda_2)\times\rho(r)$ in a.u.].

from a homogeneous electronic distribution. In the 2D plots of the RDG *vs* $sign(\lambda_2)\times\rho(r)$ shown in Figure 5b, the non-covalent attractive contacts signaled by the AIM analysis clearly appear as the peaks in the range of $sign(\lambda_2)\times\rho(r)$ between 0 and −0.01 $e{\cdot}a_0^{-3}$, colored as typical for van der Waals interactions. In keeping with the above-noted effects of solvation on the topology of the $\rho(r)$, the graphs are, essentially, indistinguishable for the complexes in DMSO and water, but slightly different for the complex in the gaseous phase. The preferential involvement of the Pd and C atoms in the stabilization of $(PdL)_2$ is also clearly noted by examining the 3D graphs plotted in Figure 5c showing the RDG = 0.5 isosurface plotted in the molecular space and colored as a function of the $sign(\lambda_2)\times\rho(r)$. The Pd–Pd and C–C contacts appear as the lighter green regions, separated by darker adjacent green regions. In the latter ones, the $sign(\lambda_2)\times\rho(r)$ is still negative, and informative about the occurrence of weak contacts involving also the N atoms of the two layers. Thus, even though the latter atoms are not connected to the surrounding ones by BPs, they still contribute to the overall stability of $(PdL)_2$. This situation is not uncommon, for complexes held together by weak van der Waals interactions. Just for instance, similar systems like palladium(II) chalcogenolate compounds, when characterized by both X-ray crystallography and DFT computations with AIM decomposition[60] report very similar interaction patterns as those previously observed in Table 1.

Finally, we also addressed the $(PdL)_2$ system in its lowest-energy triplet spin multiplicity with the target of investigating conformational changes activated by relaxation dynamics following electronic excitations. The 3D plot of the RDG *vs* $sign(\lambda_2)\times\rho(r)$ of the $^3(PdL)_2$ molecular system in DMSO (in Figure 6a) resembles that already depicted in Figure 5c. However, the investigated system in its triplet excited state lying at +47.33 kcal/mol features a shorter Pd–Pd distance by 0.2 Å at C-PCM/UB3LYP(D3)/VTZ level of theory. Interestingly we note that the shortening of such a structural parameter is due to the establishment of a weak covalent interaction between Pd–Pd atoms in two different sub-units [at the BCP, the $H(r) = -0.00046$ hartree$\cdot a_0^{-3}$ with an electronic density of 0.01405 $e{\cdot}a_0^{-3}$]. In this context, the drastic increase in $^3(PdL)_2$ potential energy is basically ascribed to destabilizing π→π repulsion effects particularly effective at shorter distances. Moreover, this trend is further supported by the Electron Localization Function (ELF) plot – between 0.0 and 0.5 – reported in panel b of Figure 6. A graphical representation of this function is capable to give a qualitative picture of the type of bonds in a molecular system and the local regions of the space where it is possible to find electron pairs.[61] In this respect, looking at the ELF sampled values over the σ[(Pd–Pd–N)-H] plane, the Pd–Pd atoms show a partially covalent connection given by the overlap of d_z^2 atomic orbitals. At the BCP connecting the two Pd atoms, the ELF features a value at around 0.14; on the contrary, the same value results substantially lower (< 0.04) for the same interaction pattern in DMSO dilute solution over the singlet electronic ground state. These last analyses – carried out over the first triplet excited state of PdL_2 most likely engaged in the clinical photodynamic therapy (PDT) of type 1 mechanism[26] – support for the first time the idea that such a light-sensitive anticancer

Table 1. Electron density $\rho(r)$ ($e\ a_0^{-3}$), Laplacian of electron density $\nabla^2\ \rho(r)$ ($e\ a_0^{-5}$), electron kinetic energy density $G(r)$ (hartree a_0^{-3}), electron potential energy density $V(r)$ (hartree a_0^{-3}), and electron energy density $H(r)$ (hartree a_0^{-3}) for bond critical points on selected bond paths (BPs) of $(PdL)_2$ calculated at the MP2/cc-pVTZ level of theory in the gas phase, in dimethyl sulfoxide (DMSO), and in water.

BP	Connected atoms		ρ(r)	$\nabla^2\rho(r)$	G(r)	V(r)	−G(r)/V(r)	H(r)
1	Pd–Pd	Gas	0.0102	0.0230	0.00569	−0.00563	1.011	0.0000634
		DMSO	0.00933	0.0205	0.00501	−0.00489	1.025	0.0001161
		Water	0.00931	0.0204	0.00499	−0.00488	1.023	0.000116
2	C–C	Gas	0.00733	0.0230	0.00458	−0.00341	1.343	0.00117
		DMSO	0.00660	0.0204	0.00401	−0.00291	1.378	0.00110
		Water	0.00659	0.0204	0.00400	−0.00291	1.375	0.00110
3	C–C	Gas	0.00479	0.0156	0.00291	−0.00193	1.508	0.000985
		DMSO	0.00478	0.0148	0.00275	−0.00181	1.519	0.000947
		Water	0.00478	0.0148	0.00276	−0.00181	1.525	0.000948
4	C–C	Gas	0.00733	0.0230	0.00458	−0.00342	1.339	0.00117
		DMSO	0.00653	0.0201	0.00395	−0.00286	1.381	0.00108
		Water	0.00652	0.0201	0.00394	−0.00285	1.382	0.00108
5	C–C	Gas	0.00525	0.0162	0.00303	−0.00201	1.507	0.00101
		DMSO	0.00518	0.0156	0.00292	−0.00194	1.505	0.000975
		Water	0.00518	0.0156	0.00292	−0.00194	1.505	0.000975
6	C–C	Gas	0.00588	0.0182	0.00351	−0.00249	1.410	0.00103
		DMSO	0.00442	0.0137	0.00258	−0.00172	1.500	0.000852
		Water	0.00440	0.0136	0.00256	−0.00171	1.497	0.000849
7	C–C	Gas	0.00440	0.0151	0.00282	−0.00187	1.508	0.000947
		DMSO	0.00450	0.0150	0.00278	−0.00180	1.544	0.000980
		Water	0.00450	0.0150	0.00278	−0.00180	1.544	0.000980
8	C–C	Gas	0.00587	0.0181	0.00350	−0.00248	1.411	0.00103
		DMSO	0.00459	0.0140	0.00265	−0.00180	1.472	0.000856
		Water	0.00457	0.0140	0.00264	−0.00180	1.467	0.000852
9′	C–H	Gas	0.00409	0.0138	0.00255	−0.00166	1.536	0.000892
10′	C–H	Gas	0.00411	0.0138	0.00256	−0.00166	1.542	0.000893
11′	C–C	Gas	0.00478	0.0156	0.00291	−0.00193	1.508	0.000984
12′	C–C	Gas	0.00525	0.0162	0.00303	−0.00201	1.507	0.00101
9	C–C	DMSO	0.00429	0.0144	0.00267	−0.00173	1.543	0.000942
		Water	0.00429	0.0145	0.00267	−0.00173	1.543	0.000944
10	C–C	DMSO	0.00367	0.0126	0.00233	−0.00150	1.553	0.000826
		Water	0.00367	0.0126	0.00233	−0.00150	1.553	0.000826
11	C–C	DMSO	0.00469	0.0143	0.00266	−0.00175	1.520	0.000917
		Water	0.00469	0.0143	0.00266	−0.00175	1.520	0.000916
12	C–C	DMSO	0.00428	0.0143	0.00266	−0.00173	1.538	0.000925
		Water	0.00428	0.0143	0.00266	−0.00173	1.538	0.000926
13	C–C	DMSO	0.00530	0.0159	0.00299	−0.00201	1.488	0.000986
		Water	0.00530	0.0159	0.00299	−0.00201	1.488	0.000986

drug might finely modulate its intermoieties distance during phototherapeutic applications. Such a modulation should potentially reflect different chemical interaction patterns between metal atoms when passing from ground to excited states.

4. Conclusions

We employed here a quantum mechanics approach to investigate a recently released potentially relevant light-activated anticancer drug for clinical photodynamic applications. Our results essentially suggest that the experimentally observed remarkable changes in the UV/Vis absorption spectra of PdL in DMSO solution or in DMSO:water mixtures can be directly

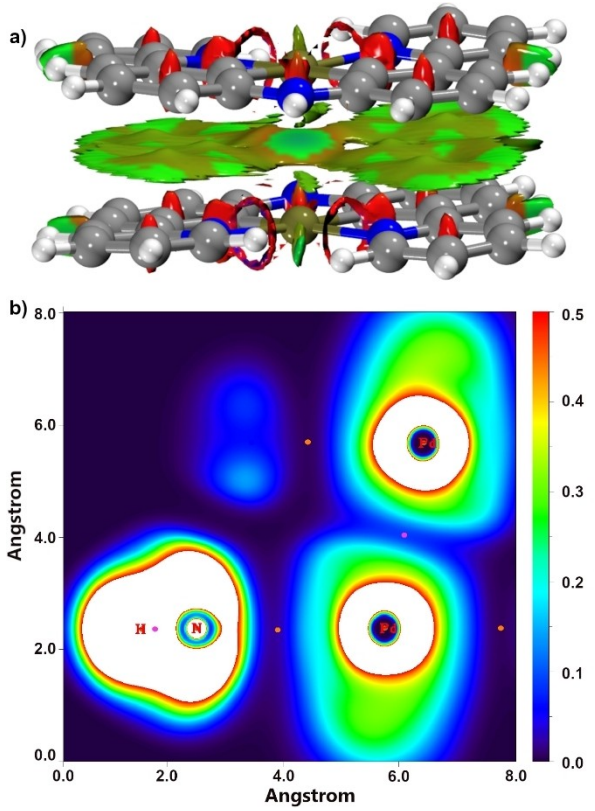

Figure 6. a) 3D Reduced Gradient Density plot – at C-PCM/UB3LYP(D3)/VTZ in DMSO – of the $^3(PdL)_2$ system with the color bar representing the $sign(\lambda_2)\times\rho(r)$ in a. u.; b) Electron Localization Function in the range 0–0.5 over a plane defined by Pd–Pd–N(H) atomic positions in the $^3(PdL)_2$ molecular system.

associated with nanostructure formations. In this respect, TD-DFT/C-PCM computations reproduce well the main adsorption pathways for both monomeric and dimeric form of PdL, shedding light on the electronic degrees of freedom responsive to light radiation. At last, the results herein reported reinforce the recent observations derived in vivo and in different contexts that supramolecular forces are effectively driving the formation of $(PdL)_2$ from one-dimensional self-assembly of PdL molecules. The stabilizing interactions are non-covalent in nature, as ascertained by an unbiased approach based on the study of the topology of the electron density and its derived reduced density gradient. The overall ensuing effect is that of slightly modulating photodynamics responses and intermoieties distances of PdL nanoparticles while maintaining the observed anticancer activity.

5. Supporting Information Summary

DFT/C-PCM optimized geometries of the PdL and $(PdL)_2$ molecular systems in their electronic ground state. We also include: *i)* the wfx output files for $(PdL)_2$; *ii)* the BCP properties – within txt files – computed with the Multiwfn program.

Acknowledgements

This work was supported by the Rome Technopole foundation within the PNRR action in the field of the NextGenerationEU – Section 4. "Digital, Industry and Aerospace". We thank the University of Tuscia for making available the DIBAF Cluster HPC Infrastructure used to perform the calculations. Open Access publishing facilitated by Università degli Studi della Tuscia, as part of the Wiley - CRUI-CARE agreement.

Conflict of Interests

The authors declare no conflict of interest.

Data Availability Statement

The data that support the findings of this study are available in the supplementary material of this article.

Keywords: Skin melanoma tumour · Anticancer drugs · Quantum mechanics · Environmental effects

[1] F. P. Pruchnik, S. A. Duraj, Introduction to Organometallic Chemistry, in *Organometallic Chemistry of the Transition Elements*, Modern Inorganic Chemistry, Chapter 1, 1-21, Springer, Boston, MA **1990**.
[2] B. Vasishta, *Essentials of Coordination Chemistry: A Simplified Approach with 3D Visuals*, Academic Press, **2015**.
[3] a) J. P. Mészáros, V. F. S. Pape, G. Szakács, G. Németi, M. Dénes, T. Holczbauer, N. V. May, E. A. Enyedy, *Dalton Trans.* **2021**, *50*, 8218–8231; b) Y. C. Ong, G. Gasser, *Drug Discovery Today: Technol.* **2020**, *37*, 17–124
[4] Z. Liu, I. Romero-Canelón, A. Habtemariam, G. J. Clarkson, P. J. Sadler, *Organometallics* **2014**, *33*, 5324–5333.
[5] D. J. Cardin, B. Cetinkaya, M. F. Lappert, *Chem. Rev.* **1972**, *72*, 545–574.
[6] P. A. Kumandin, A. S. Antonova, R. A. Novikov, K. A. Vasilyev, M. A. Vinokurova, M. S. Grigoriev, A. P. Novikov, D. K. Polianskaia, K. B. Polyanskii, F. I. Zubkov, *Organometallics* **2023**, *42*, 218–234.
[7] T. M. Trnka, R. H. Grubbs, *Acc. Chem. Res.* **2001**, *34*, 18–29.
[8] A. Kumar, B. Avula, S. Yadav, Y. Singh, S. Eraganaboyina, G. V. Zyryanov, B. R. Nemallapudi, A. K. Singh, R. Bhimireddi, *Inorg. Chem. Commun.* **2023**, *158*, 111567.
[9] D. P. Mishra, B. Acharya, S. Tripathy, B. Barik, P. K. Sahu, *Chem. Phys. Impact* **2023**, *7*, 100326.
[10] C. Copéret, A. Comas-Vives, M. P. Conley, D. P. Estes, A. Fedorov, V. Mougel, H. Nagae, F. Núñez-Zarur, P. A. Zhizhko, *Chem. Rev.* **2016**, *116*, 323–421.
[11] *Medicinal Organometallic Chemistry* (Part of the book series: Topics in Organometallic Chemistry), 1st ed., (Eds: G. Jaouen, N. Metzler-Nolte), Springer Berlin, Heidelberg, Germany, Vol. 32, **2010**.
[12] L. Kelland, *Nat. Rev. Cancer* **2007**, *7*, 573–584.
[13] Z. Lei, L. Yueshan, X. Liang, W. Wenjing, W. Ming, Y. Ting, Y. Wei, T. Chenyu, M. Zhuang, W. Tianqi, Y. Shengyong, *Signal Transduc. Target. Ther.* **2021**, *6*, 201.
[14] P. L. Bedard, D. M. Hyman, M. S. Davids, L. L. Siu, *Lancet* **2020**, *395*, 1078–1088.
[15] V. Schirrmacher, *Int. J. Oncol.* **2019**, *54*, 407–419.
[16] M. B. Lustberg, N. M. Kuderer, A. Desai, C. Bergerot, G. H. Lyman, *Nat. Rev. Clin. Oncol.* **2023**, *20*, 527–542.
[17] B. A. Chabner, T. G. Roberts, *Nat. Rev. Cancer* **2005**, *5*, 65–72.
[18] P. Martins, M. Marques, L. Coito, A. J. Pombeiro, P. V. Baptista, A. R. Fernandes, *Anticancer Agents Med. Chem.* **2014**, *14*, 1199–1212.
[19] K. Peng, Y. Zheng, W. Xia, Z.-W. Mao, *Chem. Soc. Rev.* **2023**, *52*, 2790–2832.
[20] Z. G. Chen, *Trends Mol. Med.* **2010**, *16*, 594–602.

[21] M. Zeinali, S. Abbaspour-Ravasjani, M. Ghorbani, A. Babazadeh, T. Soltanfam, A. C. Santos, H. Hamishehkar, M. R. Hamblin, *Drug Discov. Today* **2020**, *25*, 1416–1430.
[22] L. Kranz, M. Diken, H. Haas, S. Kreiter, C. Loquai, K. C. Reuter, M. Meng, D. Fritz, F. Vascotto, H. Hefesha, C. Grunwitz, M. Vormehr, Y. Hüsemann, A. Selmi, A. N. Kuhn, J. Buck, E. Derhovanessian, R. Rae, S. Attig, J. Diekmann, R. A. Jabulowsky, S. Heesch, J. Hassel, P. Langguth, S. Grabbe, C. Huber, Ö. Türeci, U. Sahin, *Nature* **2016**, *534*, 396–401.
[23] T. M. Allen, P. R. Cullis, *Science* **2004**, *303*, 1818–1822.
[24] S. Y. Qin, A. Q. Zhang, S. X. Cheng, L. Rong, X. Z. Zhang, *Biomaterials* **2017**, *112*, 234–247.
[25] L. Taoxia, C. Guo, S. Xu, G. Hu, L. Wang, *Adv. Healthcare Mater.* **2023**, *12*, 2300883.
[26] X. Q. Zhou, P. Wang, V. Ramu, L. Zhang, S. Jiang, X. Li, S. Abyar, P. Papadopoulou, Y. Shao, L. Bretin, M. A. Siegler, F. Buda, A. Kros, J. Fan, X. Peng, W. Sun, S. Bonnet, *Nat. Chem.* **2023**, *15*, 980–987.
[27] V. Petrova, M. Annicchiarico-Petruzzelli, G. Melino, I. Amelio, *Oncogenesis* **2018**, *7*, 10.
[28] Y.-Y. Wang, Y.-C. Liu, H. Sun, D.-S. Guo, *Coord. Chem. Rev.* **2019**, *395*, 46–62.
[29] B. Lu, L. Wang, H. Tang, D. Cao, *J. Mater. Chem. B* **2023**, *11*, 4600–4618.
[30] B. Yang, Y. Chen, J. Shi, *Chem. Rev.* **2019**, *119*, 4881–4985.
[31] X. Li, J. F. Lovell, J. Yoon, X. Chen, *Nat. Rev. Clin. Oncol.* **2020**, *17*, 657–674.
[32] V. W.-W. Yam, V. K.-M. Au, S. Y.-L. Leung, *Chem. Rev.* **2015**, *115*, 7589–7728.
[33] M. H.-Y. Chan, V. W.-W. Yam, *J. Am. Chem. Soc.* **2022**, *144*, 22805–22825.
[34] Y.-J. Wang, X.-Y. Shi, P. Xing, S.-Q. Zang, *J. Am. Chem. Soc. Au* **2023**, *3*, 565–574.
[35] W. J. Hehre, L. Random, P. V. R. Schleyer, J. A. Pople, *Ab Initio Molecular Orbital Theory*, John Wiley & sons Ltd., New York **1986**.
[36] W. Kohn, A. D. Becke, R. G. Parr, *J. Phys. Chem.* **1996**, *100*, 12974–12980
[37] T. M. Henderson, B. G. Janesko, G. E. Scuseria, *J. Chem. Phys.* **2008**, *128*, 194105.
[38] J. P. Perdew, K. Burke, M. Ernzerhof, *Phys. Rev. Lett.* **1996**, *77*, 3865.
[39] C. Adamo, V. Barone, *J. Chem. Phys.* **1989**, *110*, 6158–6170.
[40] A. D. Becke, *Phys. Rev. A* **1988**, *38*, 3098–3100.
[41] C. Lee, W. Yang, R. G. Parr, *Phys. Rev. B* **1988**, *37*, 785–789.
[42] S. H. Vosko, L. Wilk, M. Nusair, *Can. J. Phys.* **1980**, *58*, 1200–1211.
[43] S. Grimme, A. Hansen, J. G. Brandenburg, C. Bannwarth, *Chem. Rev.* **2016**, *116*, 5105–5154.
[44] T. H. Dunning, *J. Chem. Phys.* **1989**, *90*, 1007–1023.
[45] K. A. Peterson, D. Figgen, M. Dolg, H. Stoll, *J. Chem. Phys.* **2007**, *126*, 124101.
[46] M. Douglas, N. Kroll, *Ann. Phys.* **1974**, *82*, 89–155.
[47] B. Hess, *Phys. Rev. A* **1986**, *33*, 3742–3748.
[48] M. Cossi, N. Rega, G. Scalmani, V. Barone, *J. Comput. Chem.* **2003**, *24*, 669–681.
[49] N. M. O'Boyle, A. L. Tenderholt, K. M. Langner, *J. Comput. Chem.* **2008**, *29*, 839–845.
[50] R. E. Stratmann, G. E. Scuseria, M. J. Frisch, *J. Chem. Phys.* **1998**, *109*, 8218–8224.
[51] Gaussian 16, Revision C.01, M. J. Frisch, G. W. Trucks, H. B. Schlegel, G. E. Scuseria, M. A. Robb, J. R. Cheeseman, G. Scalmani, V. Barone, G. A. Petersson, H. Nakatsuji, X. Li, M. Caricato, A. V. Marenich, J. Bloino, B. G. Janesko, R. Gomperts, B. Mennucci, H. P. Hratchian, J. V. Ortiz, A. F. Izmaylov, J. L. Sonnenberg, D. Williams-Young, F. Ding, F. Lipparini, F. Egidi, J. Goings, B. Peng, A. Petrone, T. Henderson, D. Ranasinghe, V. G. Zakrzewski, J. Gao, N. Rega, G. Zheng, W. Liang, M. Hada, M. Ehara, K. Toyota, R. Fukuda, J. Hasegawa, M. Ishida, T. Nakajima, Y. Honda, O. Kitao, H. Nakai, T. Vreven, K. Throssell, J. A. Montgomery Jr., J. E. Peralta, F. Ogliaro, M. J. Bearpark, J. J. Heyd, E. N. Brothers, K. N. Kudin, V. N. Staroverov, T. A. Keith, R. Kobayashi, J. Normand, K. Raghavachari, A. P. Rendell, J. C. Burant, S. S. Iyengar, J. Tomasi, M. Cossi, J. M. Millam, M. Klene, C. Adamo, R. Cammi, J. W. Ochterski, R. L. Martin, K. Morokuma, O. Farkas, J. B. Foresman, D. J. Fox, Gaussian, Inc., Wallingford CT, **2016**.
[52] W. Humphrey, A. Dalke, A. K. Schulten, *J. Mol. Graphics* **1996**, *14*, 33–38.
[53] a) R. F. W. Bader, *Chem. Rev.* **1991**, *91*, 893; b) R. F. W. Bader, in *Atoms in Molecules: A Quantum Theory*, Oxford University Press, Oxford **1990**; c) F. Cortés-Guzmán, J. I. Rodríguez, and J. S. M. Anderson, in *Advances in Quantum Chemical Topology Beyond QTAIM* (Eds. J. I. Rodríguez, F. Cortés-Guzmán, J. S. M. Anderson), Elsevier Inc., **2023**, 1–19; d) P. Macchi, A. Sironi, *Coord. Chem. Rev.* **2003**, *238*, 383–412.
[54] C. Møller, M. S. Plesset, *Phys. Rev.* **1934**, *46*, 618–622.
[55] E. R. Johnson, S. Keinan, P. Mori-Sanchez, J. Contreras-Garcia, A. J. Cohen, W. Yang, *J. Am. Chem. Soc.* **2010**, *132*, 6498–6506.
[56] C. Narth, Z. Maroun, R. A. Boto, R. Chaudret, M. L. Bonnet, J.-P. Piquemal J. Contreras-García, A Complete NCI Perspective: From New Bonds to Reactivity, in *Applications of Topological Methods in Molecular Chemistry*, part of the book series: Challenges and Advances in Computational Chemistry and Physics,Vol. *22*, (Eds: R. Chauvin, C. Lepetit, B. Silvi, E. Alikhani), Springer Cham, **2016**, 491-527.
[57] T. Lu, F. Chen, *J. Comput. Chem.* **2012**, *33*, 580–592.
[58] J. Zhang, T. Lu, *Phys. Chem. Chem. Phys.* **2021**, *23*, 20323–20328.
[59] a) J. Cioslowski, J. Karwowski, Quantum-Mechanical Theory of Atoms in Molecules: A Relativistic Formulation, in *Fundamentals of Molecular Similarity. Mathematical and Computational Chemistry* (Eds: R. Carbó-Dorca, X. Gironés, P. G. Mezey), Springer, Boston, MA **2001**, Chapter 7, pp. 101–112; b) J. S. M. Anderson, Relativistic QTAIM, in *Advances in Quantum Chemical Topology Beyond QTAIM* (Eds: J. I. Rodríguez, F. Cortés-Guzmán, J. S. M. Anderson), Elsevier, **2023**, Chapter 10, pp. 245–267; c) J. S. M. Anderson, P. W. A. Ayers, *J. Phys. Chem. A* **2011**, *115*, 13001–13006; d) J. S. M. Anderson, J. I. Rodríguez, P. W. Ayers, A. W. Götz, *J. Comput. Chem.* **2016**, *38*, 81–86; e) J. S. M. Anderson, P. W. A. Ayers, *J. Comput. Chem.* **2018**, *39*, 1051–1058; f) S. Fux, M. Reiher, Electron Density in Quantum Theory, in *Electron Density and Chemical Bonding II: Theoretical Charge Density Studies* (Ed: D. Stalke), Structure and Bonding, Vol. *147*, Springer, Berlin, Heidelberg **2011**; g) J. S. M. Anderson, J. I. Rodríguez, P. W. Ayers, D. E. Trujillo-González, A. W. Götz, J. Autschbach, F. L. Castillo-Alvarado, K. Yamashita, *Chem Eur. J.* **2019**, *25*, 2538–2544; h) L. Wang, Y. Ping, R. Momen, A. Azizi, T. Xu, J. I. Rodríguez, J. S. M. Anderson, S. R. Kirk, S. Jenkins, *Chem. Phys. Lett.* **2017**, *685*, 127–132; i) R. F. W. Bader, The Lagrangian Approach to Chemistry, in *The Quantum Theory of Atoms in Molecules: From Solid State to DNA and Drug Design* (Eds: C. F. Matta, R. J. Boyd), Wiley-VCH, New York, **2007**, pp. 35–59; j) S. Sadjadi, C. F. Matta, K. H. Lemke, I. P. Hamilton, *J. Phys. Chem. A* **2011**, *115*, 13024–13035.
[60] C. N. Cechin, A. V. Paz, P. C. Piquini, A. C. Bevilacqua, N. R. Pineda, N. V. Fagundes, U. Abram, E. S. Lang, B. Tirloni, *Polyhedron* **2020**, *177*, 114315.
[61] a) A. D. Becke, K. E. Edgecombe, *J. Chem. Phys.* **1990**, *92*, 5397–5403; b) B. Silvi, A. Savin, *Nature* **1994**, *371*, 683–686.

Manuscript received: April 10, 2024
Revised manuscript received: June 20, 2024
Accepted manuscript online: July 30, 2024
Version of record online: September 21, 2024